Powder Technology 453 (2025) 120601

Contents lists available at ScienceDirect

Powder Technology

journal homepage: www.journals.elsevier.com/powder-technology

Pore-scale prediction of transport properties in lithium-ion battery cathodes during calendering using DEM and CFD simulations

Siavash Sandooghdar [a], Jiashen Chen [b], Maryam Asachi [c], Ali Hassanpour [d], Elham Hosseinzadeh [e], Meisam Babaie [b], Masoud Jabbari [b,*]

[a] Department of Mechanical Engineering, Isfahan University of Technology, Isfahan, 84156-83111, Iran
[b] School of Mechanical Engineering, University of Leeds, Leeds, LS2 9JT, UK
[c] School of Civil Engineering, University of Leeds, Leeds, LS2 9JT, UK
[d] School of Chemical and Process Engineering, University of Leeds, Leeds, LS2 9JT, UK
[e] School of Physics, Engineering and Technology, University of York, York, YO10 5DD, UK

HIGHLIGHTS

- Modelling different battery cathode particle morphology.
- Simulating different calendering compression level.
- Predicting porous cathode properties for different calendering rates.
- Predicting electrochemical-thermal performance of related to calendering.

GRAPHICAL ABSTRACT

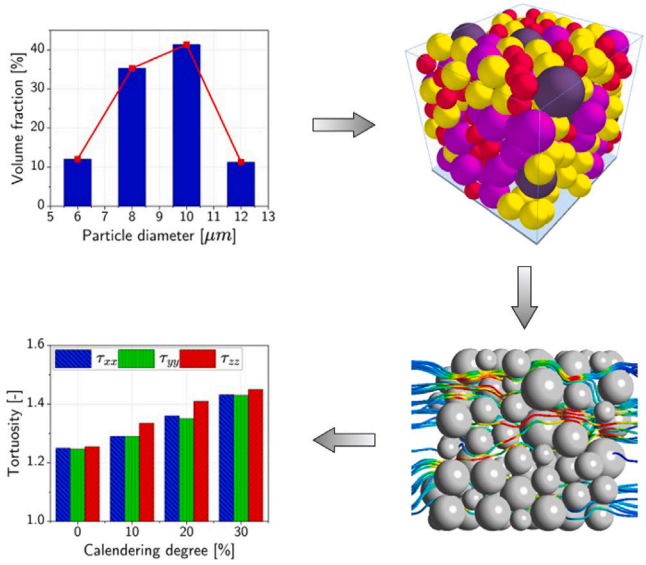

ARTICLE INFO

Keywords:
Lithium-ion batteries
Calendering
Discrete Element Method
Computational fluid dynamics
Porous media properties
Electrochemical-thermal performance

ABSTRACT

Calendering is a crucial step in the production of lithium-ion batteries (LIBs), due to its significant effect on key parameters of porous electrode structure and resultant performance. This study investigates the influence of calendering degree (compression) on porosity, tortuosity and permeability for different particle configurations. With this motivation, the mechanical behaviour of electrode structures was conducted with Discrete Element Method (DEM), and the electrolyte flow as a continuous phase was described using pore-scale computational fluid dynamics (CFD) simulations. Three different electrode microstructures were generated comprising mono-disperse and polydisperse spherical particles, as well as mono-disperse ellipsoidal particles. The predicted pore-scale properties are used in validated electrochemical–thermal models to correlate calendering process to

* Corresponding author.
E-mail address: m.jabbari@leeds.ac.uk (M. Jabbari).

https://doi.org/10.1016/j.powtec.2024.120601
Received 27 May 2024; Received in revised form 25 December 2024; Accepted 27 December 2024
Available online 3 January 2025

the overall LIB performance. The results revealed that using the ellipsoidal particles, an anisotropy in tortuosity and permeability appeared with the beginning of the compression process. As the compression degree increased to 30%, the level of anisotropy decreased, and as a consequence, the discrepancy of diagonal components of tortuosity and permeability decreased. The electrochemical–thermal models show that it is best to keep the calendering rate around 20% with smaller particle sizes (for both spherical and ellipsoidal cases).

1. Introduction

Broad applications of lithium-ion batteries (LIBs) in daily life are indisputable facts [1]. They have had a beneficial impact on energy storage field including portable devices, electronic gadgets, and transportation. A substantial increase in battery demand has led to significant efforts to improve their performance. During battery electrode production, the calendering process is a crucial step, in which the dry electrode structures are formed under pressure [2]. The calendering process — see Fig. 1(a) — improves electrical conductivity by enhancing contacts between electrode particles. It also reduces pore areas that leads to increase in the volumetric energy density. Pore-scale characteristics of the electrode structures, including porosity, tortuosity, and permeability are directly influenced by calendering [3,4] that are correlated to the LIB overall performance [5].

Alongside the experimental investigation of calendering process [6,7], numerical methods are considered as suitable tools to provide detailed insights in terms of both the mechanical aspects of the electrode structure and the electrolyte flow in the pore volume. Discrete Element Method (DEM) has demonstrated significant potential to understand the microstructure behaviour in LIB electrodes [8–11]. By combining the elasto-plastic contact model with a bond model, Giménez et al. [12] developed a DEM approach to evaluate the mechanical properties of the electrode structures. They also used the DEM simulations alongside experiments to calibrate the proposed method during compression. Using a novel DEM calendering model, Ngandjong et al. [13] studied the behaviour of the electrode meso-structure and electrochemical performance for various calendering pressures. Recently, Ge et al. [14] used DEM simulations to investigate the behaviour of electrode structures under different calendering degrees, and predicted pore-scale characteristics. They only reported bulk tortuosity using diffusive equation available by *TauFactor* application [15]. This approach, however, requires more calibration and correction to the predicted tortuosity values, especially if the volume of "closed pores" within the bulk increase [16].

Most authors have considered spherical particles to construct electrode structures in DEM simulations, however, the particles are not necessarily spherical in the real structures [17]. This would lead to change of pore-scale properties — that has been investigated in other similar areas but batteries [18,19]. The only research conducted for LIBs considering non-spherical particle shapes is the DEM simulations by Becker et al. [20]. They, however, only reported the effective transport in solid and electrolyte using resistance network (RN) method [21], which does not adequately account for the tortuous pathways that ions or electrons must travel through the pore space or solid matrix.

This study aims to investigate the effect of calendering degree on the behaviour of porous electrode microstructures for different particle configurations. i.e. mono-disperse and polydisperse spherical particles, as well as mono-disperse ellipsoidal particles. Unlike any other research for LIBs in literature, computational fluid dynamics (CFD) analysis is used to solve diffusive–convective transport of within the pore areas (whether they are closed or not) between the particles to calculate pore-scale characteristics. This allows prediction of permeability and tortuosity tensor for the microstructure than a single bulk value. Moreover, 3D electrochemical–thermal models are used to study the link between predicted porous medial properties with the downstream battery performance in terms of their optimised operating conditions.

2. Material and methods

2.1. DEM model

DEM was originally introduced by Cundall and Strack [22] to simulate the interaction between spherical particles. It has been widely applied in various fields, including agriculture, pharmaceutical, civil, etc [23–25]. Recently, DEM has also been successfully utilised to build the structure of porous media at the pore scales model. DEM describes the translational and rotational motion of an individual particle in the structure as

$$m^k \frac{d\mathbf{v}^k}{dt} = \mathbf{F}_b^k + \mathbf{F}_p^k \tag{1}$$

$$I^k \frac{d\boldsymbol{\omega}^k}{dt} = \mathbf{M}_b^k + \mathbf{M}_p^k \tag{2}$$

in which for the kth particle m and I are the mass and moment inertia, $\mathbf{v}$ is the translational velocity, $\boldsymbol{\omega}$ is the angular velocity, $\mathbf{F}_b$ is the bond force, $\mathbf{M}_b$ is the bond torque, both for describing CBD phase interaction. $\mathbf{F}_p$ explains the contact force of the neighbouring particles, $\mathbf{M}_p$ stands for the contact torque that originate from the tangential contact force and rolling friction between neighbouring particles.

In this work, the Edinburgh elasto-plastic adhesive (EEPA) model and bond model were employed to capture the interaction between active particles and inter particle binder phase, respectively. There are already several works that used the EEPA model to capture the mechanical behaviour of granular materials [14,26–30]. The normal force for the particle interaction, $\mathbf{F}_{n,p}$, is the sum of damping force, f_{nd} and hysteretic spring force, f_{hys} as follows

$$\mathbf{F}_{n,p} = \left(f_{hys} + f_{nd}\right)\mathbf{n}, \tag{3}$$

where $\mathbf{n}$ is the unit normal vector from the contact point to the particle centre. The hysteretic force–displacement relationship is given by

$$f_{hys} = \begin{cases} f_0 + k_1\delta^n & \text{when } k_2\left(\delta^n - \delta_p^n\right) \geq k_1\delta^n \\ f_0 + k_2\left(\delta^n - \delta_p^n\right) & \text{when } k_1\delta^n > k_2\left(\delta^n - \delta_p^n\right) > -k_{adh}\delta^n \\ f_0 - k_{adh}\delta^n & \text{when } k_{adh}\delta^n \geq k_2\left(\delta^n - \delta_p^n\right) \end{cases} \tag{4}$$

in which f_0 is constant adhesion force, δ is total normal overlap, δ_p is plastic overlap, k_1 is the loading stiffness, k_2 is the unloading stiffness, k_{adh} is the adhesive stiffness, and n is the non-linear index parameter that is set to 1.5 in this study [14]. The loading stiffness is calculated by $\frac{4}{3}\sqrt{R^*}E^*$ with R^* and E^* equivalent to Young's modulus and radius, respectively. The contact plasticity ratio is also calculated as $\lambda_p = 1 - (k_1/k_2)$.

The damping force is calculated by $f_{nd} = -\beta_n \upsilon_n$ with υ_n as the relative normal velocity, and β_n as the normal damping coefficient calculated by

$$\beta_n = \sqrt{\frac{4m^*k_1}{1 + (\pi/\ln e)^2}} \tag{5}$$

where e is the coefficient of restitution, and m^* is the equivalent mass of particle i and j, given by:

$$\left(m^*\right)^{-1} = \left(m_i\right)^{-1} + \left(m_j\right)^{-1} \tag{6}$$

The contact tangential force for the neighbouring particles is calculated by summing tangential spring force, $\boldsymbol{f}_{ts}$, and tangential damping force, $\boldsymbol{f}_{td}$, as $\mathbf{F}_{t,p} = \boldsymbol{f}_{ts} + \boldsymbol{f}_{td}$. The tangential spring force equals to

$$\boldsymbol{f}_{ts} = \boldsymbol{f}_{ts}^{n-1} + \Delta\boldsymbol{f}_{ts}, \tag{7}$$

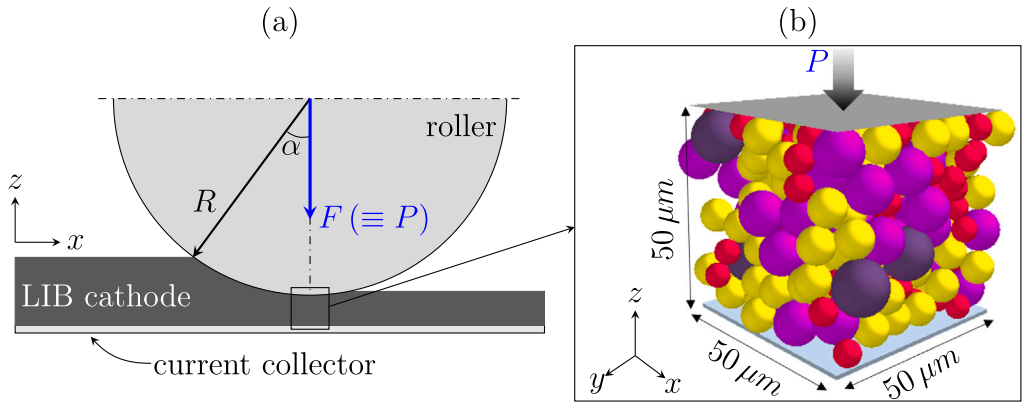

Fig. 1. (a) Schematic illustration of the calendering process, and (b) Representative Elementary Volume (REV) of the DEM simulation setup for the generation of electrode structure.

where $\boldsymbol{f}_{ts}^{n-1}$ is the force from the previous time step, and the incremental tangential force is $\Delta \boldsymbol{f}_{ts} = -k_t \boldsymbol{v}_t \Delta t$. Here, Δt is the time step, $\boldsymbol{v}_t$ is the velocity in tangential direction, and the tangential stiffness for $n = 1.5$ (in this study) is expressed as

$$k_t = 8\xi_{t,m} G^* \sqrt{R^* \delta^n}, \tag{8}$$

where G^* is the equivalent shear modulus, and $\xi_{t,m}$ is the tangential stiffness multiplier that for non-linear elastic contact springs is recommended as 2/3 [31] or 2/7 [32]. There is no recommendation in literature for a non-linear elasto-plastic normal spring, however, the study by Mohajeri et al. [33] suggests that 0.4 is a good approximation – and adopted in our study – with no significant influence on the simulation stability and simulated bulk responses for a range of case studies for $0.2 < \xi_{t,m} < 1$.

The tangential damping force is $\boldsymbol{f}_{td} = -\beta_t \boldsymbol{v}_t$, where the tangential damping coefficient is expressed as

$$\beta_t = \sqrt{\frac{4m^* k_t}{1 + (\pi / \ln e)^2}}. \tag{9}$$

The critical tangential force value is set to

$$f_{cr} \le \mu \left| f_{hys} + k_{adh} \delta^n - f_0 \right| \tag{10}$$

where μ stands for the friction parameter. The total applied torque is then expressed as $\boldsymbol{\eta}_i = -\mu_r \left| f_{hys} \right| s_i \boldsymbol{\omega}_i$ with μ_r as the rolling friction parameter, s_i as the distance from contact point to the particle centre, and $\boldsymbol{\omega}_i$ as unit angular velocity at the contact point.

For describing the mechanical response of the inter particle binder phase the initial model developed by Potyondy and Cundall [34] is used in this study, where the normal force is described as

$$\mathbf{F}_{n,b} = \mathbf{F}_{n,b}^{n-1} + \Delta \mathbf{F}_{n,b}, \quad \text{and} \quad \Delta \mathbf{F}_{n,b} = -k_{n,b} \boldsymbol{v}_{n,b} \Delta t, \tag{11}$$

where $\mathbf{F}_{n,b}^{n-1}$ is the previous time step bond force, $\Delta \mathbf{F}_{n,b}$ is the incremental normal force, $k_{n,b}$ is the bond normal stiffness, $\boldsymbol{v}_{n,b}$ is the velocity in normal direction. The tangential spring bond force is calculated in the same format as

$$\mathbf{F}_{t,b} = \mathbf{F}_{t,b}^{n-1} + \Delta \mathbf{F}_{t,b}, \quad \text{and} \quad \Delta \mathbf{F}_{t,b} = -k_{t,b} \boldsymbol{v}_{t,b} \Delta t, \tag{12}$$

with $k_{t,b}$ as bond tangential stiffness, and $\boldsymbol{v}_{t,b}$ as the tangential velocity. The normal and tangential bond moments are calculated as follows

$$\mathbf{M}_{n,b} = \mathbf{M}_{n,b}^{n-1} + \Delta \mathbf{M}_{n,b}, \quad \text{and} \quad \Delta \mathbf{M}_{n,b} = -k_{n,b} A_b \boldsymbol{\omega}_{n,b} \Delta t J_b, \tag{13}$$

$$\mathbf{M}_{t,b} = \mathbf{M}_{t,b}^{n-1} + \Delta \mathbf{M}_{t,b}, \quad \text{and} \quad \Delta \mathbf{M}_{t,b} = -k_{t,b} A_b \boldsymbol{\omega}_{t,b} \Delta t I_b, \tag{14}$$

where A_b is the bond cross sectional area, J_b and I_b are the polar moment and the moment of inertia of the bond, $\boldsymbol{\omega}_{n,b}$ and $\boldsymbol{\omega}_{t,b}$ are relative angular velocities in normal and tangential directions. Finally, for the bond breakage occurrence the maximum stress criterion is adopted, which is expressed as

$$\sigma_{n,b} = \frac{|\mathbf{F}_{n,b}|}{A_b} + \frac{|\mathbf{M}_{t,b}| R_b}{I_b} \le \sigma_{n,st}, \tag{15}$$

$$\sigma_{t,b} = \frac{|\mathbf{F}_{t,b}|}{A_b} + \frac{|\mathbf{M}_{n,b}| R_b}{J_b} \le \sigma_{t,st}, \tag{16}$$

where $\sigma_{n,b}$ and $\sigma_{t,b}$ are bond normal and shear stresses, $\sigma_{n,st}$ and $\sigma_{t,st}$ are bond normal and shear strength. All the input parameters needed for DEM simulation can be seen in Table 1 [10,14].

Table 1
DEM simulation input parameters for $LiNi_{0.6}Co_{0.2}Mn_{0.2}O_2$ (NMC)-622 cathodes [10,14].

Parameter	Value
Particle density, ρ_p	4740 kg/m^3
Young's modulus, E_p	75 GPa
Poisson ratio, ν_p	0.25
Coefficient of restitution, e	0.25
Particle static friction, $\mu_{p,s}$	0.12
Particle rolling friction, $\mu_{p,r}$	0.01
Plate Young's modulus (Steel), E_{St}	208 GPa
Plate density (Steel), ρ_{St}	7900 kg/m^3
Plate Poisson's ratio (Steel), ν_{St}	0.3
Plate Young's modulus (Aluminium), E_{Al}	69 GPa
Plate density (Aluminium), ρ_{Al}	2700 kg/m^3
Plate Poisson's ratio (Aluminium), ν_{Al}	0.3

2.2. DEM and electrode structures generation

DEM simulations in this study were conducted using Altair EDEM as a high-performance tool for granular material simulation. The $LiNi_{0.6}Co_{0.2}Mn_{0.2}O_2$ (NMC)-622 cathodes is considered as the active particle, which was chosen from the work by Zhang et al. [10]. To generate the porous electrode structures, after the modelling a cuboid domain, particles fall under the influence of gravity from the top surface randomly. The size of the computational domain used in our DEM simulations is set to 50 μm×50 μm×50 μm [35,36]. As shown in Fig. 1(b), the particles were confined between two parallel plates. The top steel plate was movable to compress particles along the z-direction with a constant velocity of 0.01 m/s and the bottom aluminium plate was fixed [14]. For the sides (x and y directions), the periodic boundary conditions were imposed. The bonds were applied to the active material before calendering. The bonds play an essential role at the beginning of the calendering process. Due to the presence of micron-sized particles, a time step of 1×10^{-10} s was employed for all DEM simulations.

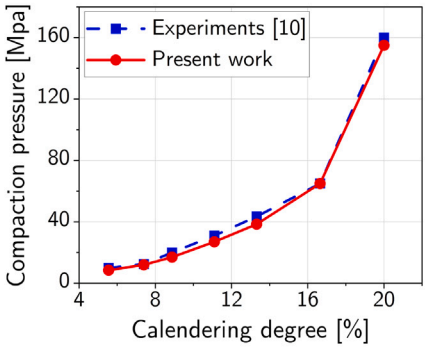

Fig. 2. Comparison of experimental and DEM simulation nanoindentation curve.

2.3. Verification of DEM simulation

To validate the DEM simulation, the experimental nanoindentation measurements from Zhang et al. [10] are utilised, which provided the pressure–displacement curves. In the research performed by Schreiner et al. [28], the normal-shear stress and surface energy were known as effective parameters in the calibration of the compression process. In the present work, we set the bonding parameters to calibrate the compaction behaviour of the electrode. The bond stiffness k_b values and the bond strength σ_n values are achieved 1×10^{14} N/m^3 and 1×10^{8} Pa, respectively. As illustrated in Fig. 2, the compaction behaviour captured in DEM simulations showed good agreement with the literature data [10].

2.4. Particle morphology

To evaluate the effect of electrode microstructure configuration on transport properties, the mono-disperse, polydisperse spherical particles, and the mono-disperse non-spherical particles are considered (Fig. 3). In this study, the particle size ranges from 6 to 12 μm, which is mostly considered as the size of AM particles [10,11,14,37]. Within the mono-disperse spherical particles, four different diameters, 6, 8, 10, and 12 μm, are investigated. The number of particles in each assembly with the particle diameters of 6 μm, 8 μm, 10 μm, and 12 μm were 640, 270, 137, and 60, respectively. As illustrated in Fig. 3(d), the particle size distribution by diameter, which varies from 6 μm to 12 μm, is applied to the case of the polydispersed spherical particle. This case consists of 247 particles.

To avoid the simplified spherical particles for the electrode structures and observe the effect of the deviations from sphericity, the mono-dispersed ellipsoidal particles are considered as the oriented particles. Similar to the case of mono-disperse spheres, four different types of mono-dispersed ellipsoidal particles were created to examine particle size effects. Here, an ellipsoid particle is defined with a length axis c, a short axis a, and an aspect ratio $AR = c/a$. The values of the short diameters of the ellipsoidal particles were 6 μm, 8 μm, 10 μm, and 12 μm, which were the same as the spherical diameters. All ellipsoidal particles used in this work were produced with the aspect ratio of 1.5. The number of particles in each assembly with the short diameters of 6 μm, 8 μm, 10 μm, and 12 μm were 460, 197, 102, and 55, respectively.

To build the ellipsoidal particles, the multiple-sphere method is used in the DEM simulations. In this method, a composition of sub-spheres with different radii and levels of overlapping are inscribed into a non-spherical particle. The accuracy of the multi-sphere method can be influenced by the number, radii, and positions of the sub-spheres inside the non-spherical particle. As discussed in previous studies [38,39] a better estimation of the ellipsoid surface may provide more accurate results. In this work, the 9-sphere model is employed to represent an ellipsoidal particle similar to that reported by Lin et al. [40], who studied the mechanical response of ellipsoidal particles under confined compression. Fig. 4 illustrates the positions of the sub-spheres inside an ellipsoidal particle, which are tangent to it.

2.5. CFD analysis

To investigate the electrode structure characteristics, the flow behaviour of the liquid electrolyte in the porous electrode is analysed using CFD based on finite volume methods (FVM). All the CFD computations were performed using the ANSYS CFX software under steady state conditions. Therefore, the impact of different compression rates on porosity, tortuosity, and permeability was explored using CFD analysis. To construct the fluid domain for the CFD simulations, the generated electrode structure from the DEM simulation was imported into ANSYS Design Modeller. For the ellipsoidal particles, the centre of particles and their orientation tensors were exported into the Design Modeller. Single-phase incompressible flow of electrolyte through the domain is considered by solving the mass and momentum conservation equations follows [41]:

$$\nabla \cdot \mathbf{u} = 0 \tag{17}$$

$$\frac{\partial \mathbf{u}}{\partial t} + (\mathbf{u}\cdot\nabla)\,\mathbf{u} = -\frac{1}{\rho}\nabla p + \nabla\cdot\boldsymbol{\tau} + \mathbf{g} + \mathbf{f}, \tag{18}$$

where $\mathbf{v}$ is the velocity vector, t is time, ρ is the density, p is the pressure, $\boldsymbol{\tau}$ is the deviatoric stress tensor, ∇ denotes the vector differential, and $\mathbf{g}$ is the gravitational acceleration vector (which is neglected in this study), and $\mathbf{f}$ is the momentum source term for flow in porous media. Neglecting elastic behaviour, the viscous deviatoric stress tensor becomes

$$\boldsymbol{\tau} = 2\mu\mathbf{D}, \tag{19}$$

in which μ is the dynamic viscosity, $\mathbf{D} = \left(\nabla\mathbf{u} + \nabla\mathbf{u}^{\top}\right)$ is the deformation rate tensor, and $\top$ is the transpose notation.

An example of flow (streamlines coloured by the velocity magnitude) with boundary conditions are shown in Fig. 5. Uniform inlet velocity is considered on the inlet boundary. Periodic boundaries are applied on the surfaces parallel to flow direction. No-slip condition is adopted on the particle walls (interfaces). In this work, the Reynolds number, Re, was considered 0.001 in all cases. The electrolyte properties were chosen from [42], with a density of 1300 kg/m^3 and a dynamic viscosity of 3.2 mPa·s.

An unstructured mesh is applied to 3D complex porous geometry, which is shown in Fig. 6(a). To investigate the grid independence, the number of elements is varied from 1,925,000 to 7,323,000 in four steps. There is no significant variation in pressure drop for cell numbers of more than 5,209,000 as illustrated in Fig. 6(b), hence, this has been used for the CFD simulations.

2.6. Calculation of transport properties

2.6.1. Porosity

As mentioned before, the particle arrangements are imported into ANSYS Design Modeller before and after calendering. The pore volume can be exactly calculated by subtracting the volume of the porous structure from the cube domain. This approach is efficient even after compression, which leads to particle deformation and overlaps between soft particles. Fig. 6(a) displays the pore volume of the electrode structure. The porosity of the granular structure ε is determined by:

$$\varepsilon = \frac{V_f}{V_{\text{tot.}}}, \tag{20}$$

where V_f is the pore volume, and $V_{\text{tot.}}$ is the volume of the cube domain. As seen in Fig. 7, for spherical particles with 10 μm diameter, the porosity calculated for the current study is in good agreement with the simulated results from Zhang et al. [11], which were validated by mercury intrusion porosimeter.

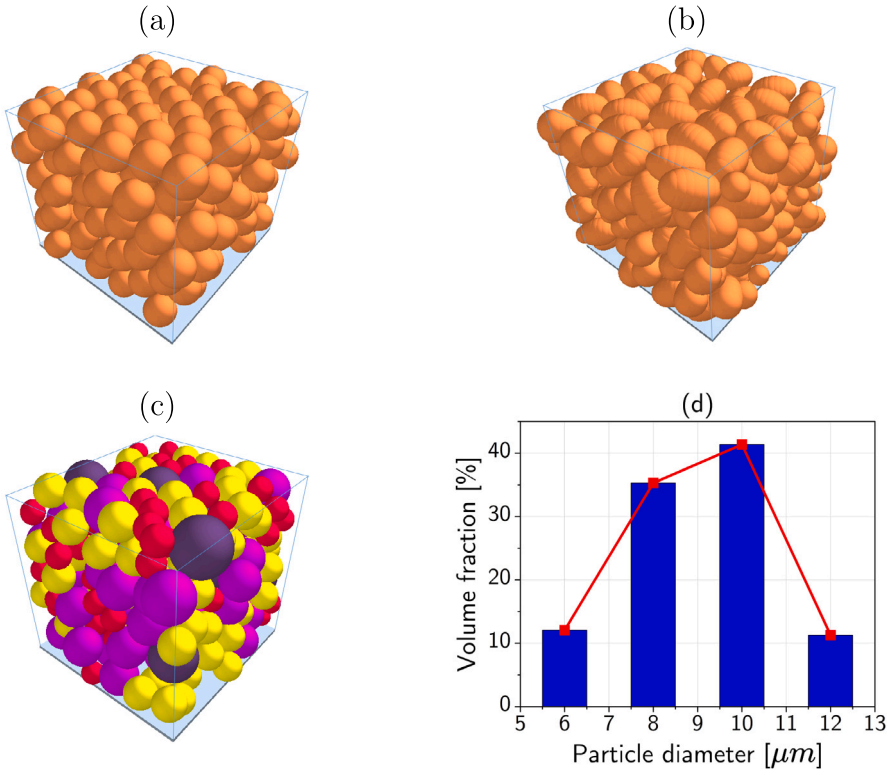

Fig. 3. Particle morphology of uncalendered electrodes: (a) mono-disperse spherical particles, (b) monodisperse non-spherical particles, (c) polydisperse spherical particles, (d) particle size distribution of polydisperse particles.

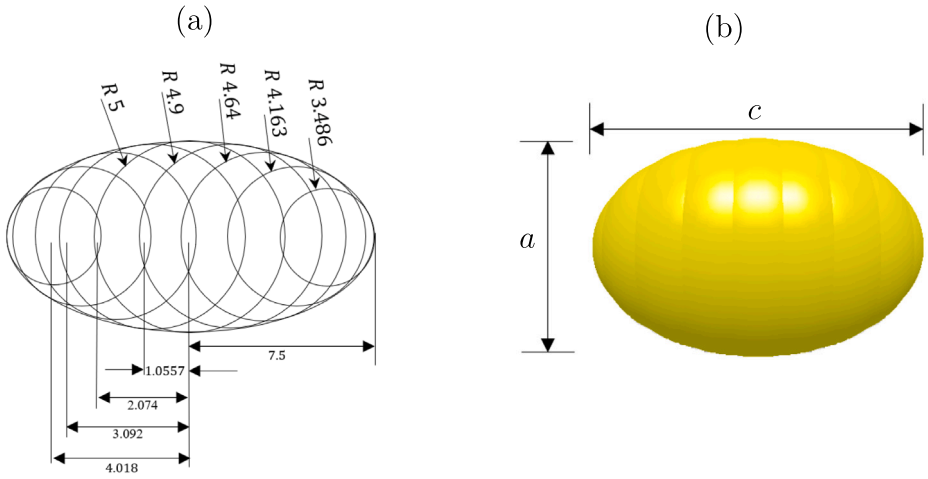

Fig. 4. (a) Multiple sphere model for representing an ellipsoidal particle with 9 sub-spheres, and (b) an example of ellipsoidal particle.

2.6.2. Tortuosity

The tortuosity factor plays a crucial role in predicting the transport properties of a porous medium [35,43,44]. In this study, the geometrical tortuosity [45] is adopted, which can be explained as:

$$\tau_{ii} = \frac{L_{g,i}}{L_{0,i}}, \quad i \in \{x, y, z\} \tag{21}$$

where for each direction of i of coordinate system L_g is the average length of the real pathways of fluid through the porous media, and L_0 is the length of the straight-line across the porous media in the direction under study. Using Eq. (21), the tortuosity factor is always greater than one. To obtain the tortuosity factor, the average length of the flow streamlines is extracted from ANSYS CFD-POST, which is shown in Fig. 8. As illustrated, L_g is the part of the flow paths, which is inside the porous media.

2.6.3. Permeability

In this study, for laminar flows through porous electrode structure, the permeability is calculated by Darcy's law and using the extra momentum source **f** added into Eq. (18), which is

$$\mathbf{f} = -\gamma \mathbf{K}^{-1}\mathbf{U} = -\mu \begin{bmatrix} \frac{1}{K_{xx}} & 0 & 0 \\ 0 & \frac{1}{K_{yy}} & 0 \\ 0 & 0 & \frac{1}{K_{zz}} \end{bmatrix} \cdot \begin{bmatrix} U_{xx} \\ U_{yy} \\ U_{zz} \end{bmatrix} \tag{22}$$

in which γ is the dynamic viscosity, **K** is the permeability vector, and U_{ii} is the volume-averaged velocity in the "i" direction.

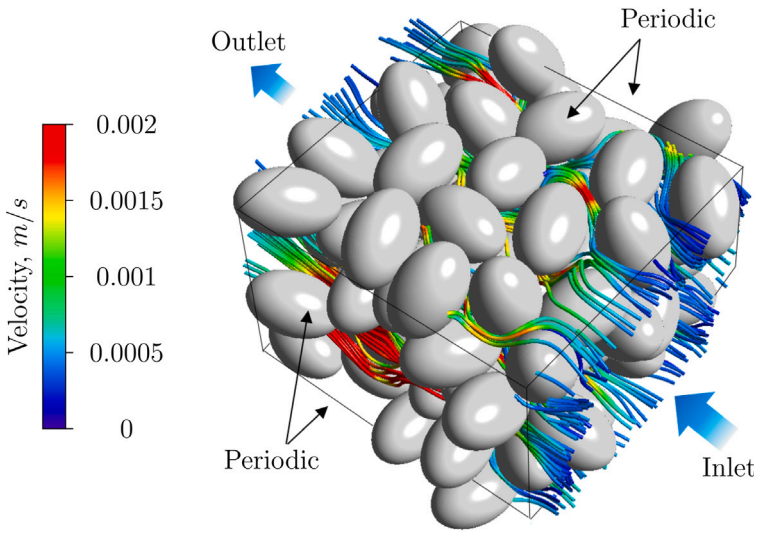

Fig. 5. An example of CFD simulation with the corresponding boundary conditions.

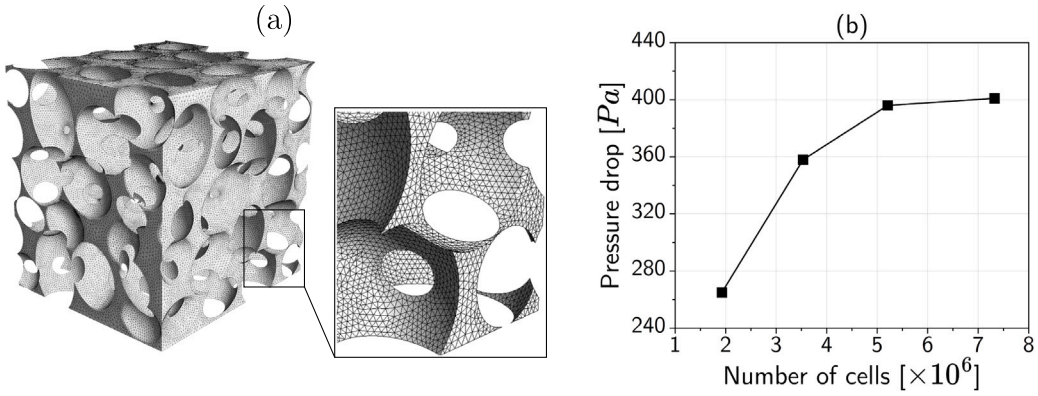

Fig. 6. (a) Unstructured mesh used for discretising porous media, and (b) mesh sensitivity analysis.

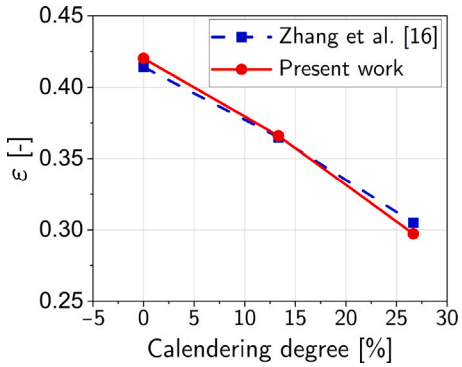

Fig. 7. Variation of porosity with the increase of calendering degree for spherical particles with 10 μm diameter.

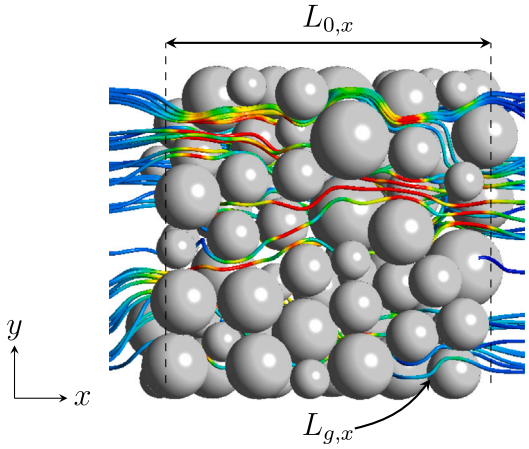

Fig. 8. Illustration of the tortuosity of streamlines in the electrode structure.

2.7. 3D electrochemical-thermal model

A validated model developed by Hosseinzadeh et al. [46–48] is used in this study for evaluating the influence of porous media properties variation on a 10 Ah lithium phosphate (LFP) battery pouch cell at 3C discharge rate in the room temperature (25 °C). The cell is assumed to be a sandwiched structure of a negative current collector, a negative electrode, a separator, a positive electrode, and a positive current collector — see Fig. 9. The electrode pore volumes (with porosity of ε) are filled with electrolyte, and the rest of it is the solid active material, ε_s, where $\varepsilon + \varepsilon_s = 1$. The key parameters that affect the kinetics of reaction in a LIB are the effective ionic conductivity, κ_i^{eff}, the effective diffusivity of electrolyte, D_e^{eff}, and the effective electronic conductivity,

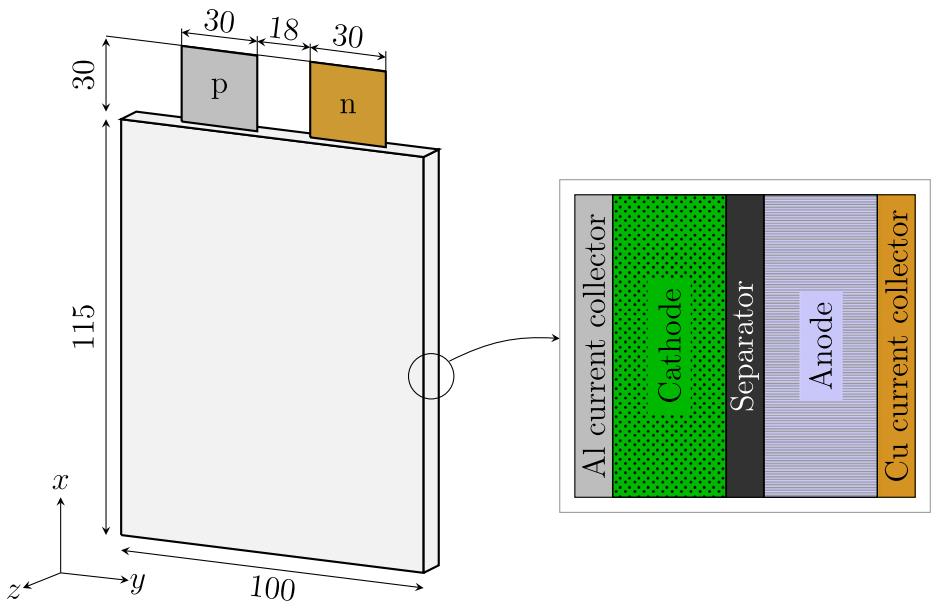

Fig. 9. Schematic illustration of the LIB cell used in this study with the sandwich structure containing the aluminium (Al) current collector, the cathode, the separator, the anode, and the copper (Cu) current collector. All the dimensions are in millimetres and based on [49].

κ_e^{eff}. These parameters are dependent on the porous properties and are used in the electrochemical-thermal model as follows

$$\kappa_i^{\text{eff}} = \frac{\kappa_i \varepsilon}{\tau} \tag{23}$$

$$D_e^{\text{eff}} = \frac{D\varepsilon}{\tau} \tag{24}$$

$$\kappa_e^{\text{eff}} = \frac{\kappa_e \varepsilon_s}{\tau} \tag{25}$$

where κ_i, D, and κ_e are the intrinsic ionic conductivity of the electrolyte, the intrinsic diffusivity, and the intrinsic electronic conductivity, respectively. For Eqs. (23)–(25), the value of porosity and tortuosity are inputted from the results of calendering modelling. The intrinsic ionic conductivity of the electrolyte is highly dependent on the lithium concentration in the electrolyte, C_{elec}, and the operation temperature, T, as follows [49]

$$\begin{aligned}\kappa_i = 1.12\times10^{-4}\big(&-82488 + 0.053248T - 2.9871\times10^{-5}T^2 + 0.26235C_{\text{elec}} \\ &- 9.3063\times10^{-3}C_{\text{elec}}T + 8.069\times10^{-6}C_{\text{elec}}T^2 + 0.22002C_{\text{elec}}^2 \\ &-1.765\times10^{-4}C_{\text{elec}}^2T\big)\end{aligned} \tag{26}$$

All other thermo-physical, electrical, and chemical properties are detailed in the original references [46–49].

3. Results and discussion

3.1. Porosity

After constructing the initial structure in DEM simulations, the top plate moved down, and the electrode structures were gradually compressed to provide various degrees of calendaring, with decreasing electrode vertical thickness. As illustrated in Fig. 10, four different calendering levels (0%, 10%, 20%, and 30%) were achieved to investigate electrode structure characteristics. This means that the electrodes thickness was reduced to 10%, 20%, and 30%, of its original thickness. As we pointed out earlier, by measuring the pore volume from the geometry required for CFD analysis, the porosities can be calculated under different calendering levels. Fig. 10 illustrates the effect of the calendering level on the porosity for various particle morphologies used in this study. In this figure, the porosity decreases with increasing calendering levels. As can be seen, the values of porosity for prolate particles are almost less than for spherical particles at each calendering degree. This behaviour, of course, is dependent on the sphericity factor, which is here 0.97 for ellipsoidal particles used with the aspect ratio of 1.5. Lower values of sphericity can lead to a higher porosity [19]. It is also observed that the porosity reduction rate increases almost after 20% compression.

3.2. Tortuosity

One of the different and significant aspects of the morphology of non-spherical particles compared to spherical particles during compression is the appearance of anisotropy in the porous medium. Although the cube was filled with random orientations at the beginning, however, during calendering, they have a tendency to lie horizontally in the direction perpendicular to the applied load. This can significantly alter the characteristics of porous electrode, including the tortuosity and permeability dependent on the direction. We measured the average inclination angle, θ, of ellipsoidal particles with respect to the horizontal xy plane at each calendering level. As can be observed in Fig. 11, the values of θ decrease with increasing compression degree.

In order to address the anisotropic transport properties of the porous electrode, we have considered the uniform flow in the xyz-directions for all morphologies. Fig. 12 illustrates the relationship between the diagonal components of tortuosity and the calendering degrees for ellipsoidal particles used in this study. As seen, the values of the tortuosity increase with increasing calendaring degree for the all ellipsoidal particle sizes. It can be observed that for the uncalendered structures, the diagonal components of tortuosity showed almost the same values for the all ellipsoidal particle sizes. As the compression process begins, an anisotropy in tortuosity starts.

As seen from Fig. 12, for 10% and 20% calendered electrodes, the value of τ_{zz} is about 5% more than τ_{xx} and τ_{yy}. In fact, as mentioned earlier, particles tend to orient horizontally in the xy plane, which is perpendicular to the applied force during compression. Therefore, the flow must pass through distorted paths in the z direction than in the x and y directions, which leads to an increase in the value of tortuosity. As the compression degree increased from 20% to 30%, the level of anisotropy decreases, and as a consequence, the discrepancy of τ_{zz} decreases.

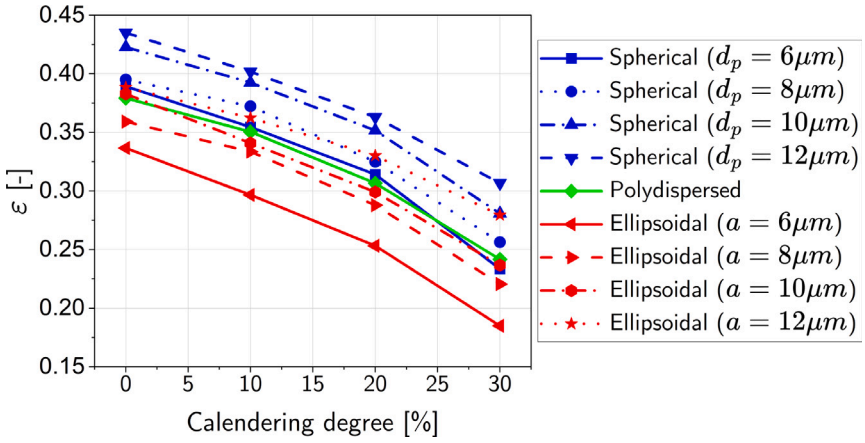

Fig. 10. Evolution of porosity under different calendering degrees.

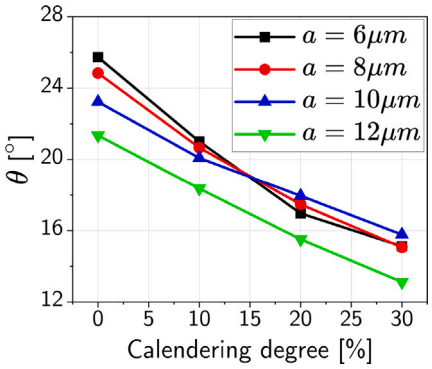

Fig. 11. Variation of the average inclination angle of ellipsoidal particles with respect to the horizontal xy plane with the increase of calendering degree.

Since the three diagonal tortuosity components have the same values in each calendering level for spherical morphologies, we have avoided to present the tortuosity components for the other two morphologies, i.e. for mono-disperse and polydisperse spherical particles. Fig. 13 shows the variation of tortuosity with different porosities (caused by different to calendering rates) for mono-disperse and polydisperse spherical particles. As seen, the values of the tortuosity decrease with increasing porosity. The values of the tortuosity have approximately the same value at each porosity for all spherical morphologies.

3.3. Permeability

Fig. 14 shows the relationship between the diagonal components of permeability and the calendering degrees for ellipsoidal particles used in this study. As illustrated in this figure, the values of the permeability decrease with increasing calendaring degree for the all ellipsoidal particle sizes. Similar to tortuosity, for the uncalendered structures, the diagonal components of permeability showed almost the same values and as the calendering process begins, an anisotropy in permeability starts. As seen, for 10% and 20% calendered electrodes, the value of K_{zz} is about 12% less than K_{xx} and K_{yy} for the all ellipsoidal particle sizes. It is obvious that a distorted path in the z direction results in less permeability. Here again, as the compression degree increased from 20% to 30%, the level of anisotropy decreases, and the diagonal components of permeability have the same value.

The three diagonal components of permeability are equal for spherical particles. Fig. 15 has shown that the variation of permeability with different porosities due to calendering process for monodisperse and polydisperse spherical particles. As seen, the permeability increases with increasing the porosity. It is also observed that for all spherical morphologies, the changes in the values of the permeability is not that significant for the porosity values less than 0.35.

3.4. Optimised LIB performance

The results of porous media properties obtained above are use in the electrochemical-thermal model to correlated the optimised LIB operating condition to the calendering degree, the particle and morphology. Example of the electrochemical-thermal results are shown in Fig. 16(a)–(c) for the spherical particles of 6 μm. The results in Fig. 16(c) show that increasing calendering degree does not change the discharge curve that much with a maximum depth of discharge (DoD) around 95%. However, the LIB surface temperature (Fig. 16(a)) as well as the average cell temperature (Fig. 16(b)) increase by calendering degree — this becomes more pronounced at 30% calendering degree. High calendering degree reduces the porosity and increases the tortuosity (distorting ion pathways). This limits electrolyte infiltration and slows ion transport, leading to higher internal resistance during operation. As a result, Ohmic heating increases, causing a rise in temperature.

The same trend — temperature rise with calendering degree — can be seen for all other particle sizes and morphologies in Fig. 17(a). This confirms that although high calendering degree densifies LIB electrodes, it does not help in terms of overall thermal performance. The results, moreover, show that increasing particle size will, in general, increase the temperature. This is mostly due to reduced solid-state diffusion through particles, which increase the internal resistance. Ellipsoidal particles, on the other hand, show lower temperatures in contract to equivalent spherical particles. Ellipsoidal particles tend to pack less efficiently, leading to higher porosity and better electrolyte wetting. This can lower internal resistance and promote heat dissipation, reducing localised temperature rise during cycling. Moreover, they create anisotropic ion pathways due to elongated geometry, improving ion transport along preferred directions. This enhanced transport reduces polarisation losses, minimising resistive heating during operation.

Fig. 17 shows that increasing calendering degree from 20% to 30% decreases the maximum DoD. This is mainly due to reduction in porosity and pore size that limits electrolyte infiltration, resulting in poor wettability and less active material being effectively utilised during discharge. Compaction, moreover, increases the tortuosity of ion diffusion pathways, making it harder for Li-ions to penetrate deep into the electrode. Higher resistance leads to polarisation losses, causing the voltage to drop prematurely before the full capacity can be accessed, effectively reducing the useable capacity (lower DoD). The results, clearly show that better DoDs are achieved for particle sizes lower than 12 μm (both spherical and ellipsoidal). In conclusion, it is apparent that

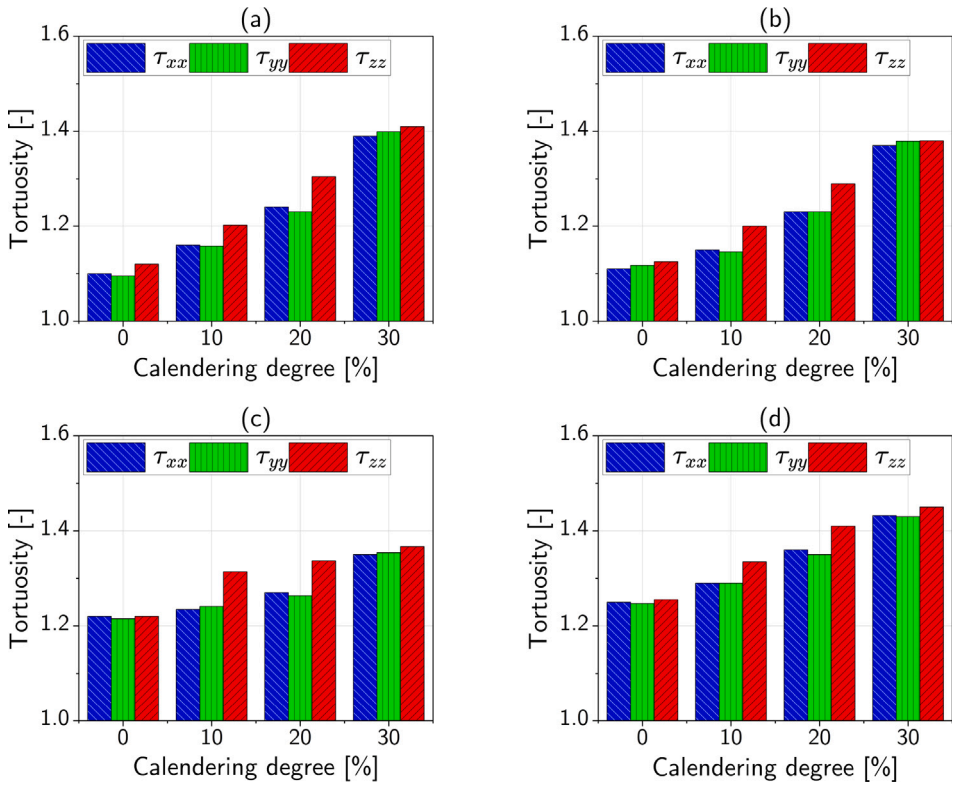

Fig. 12. Diagonal components of the tortuosity, τ_{ii} under different calendering degrees. Short axis of ellipsoidal particles a: (a) 6 μm, (b) 8 μm, (c) 10 μm, and (d) 12 μm.

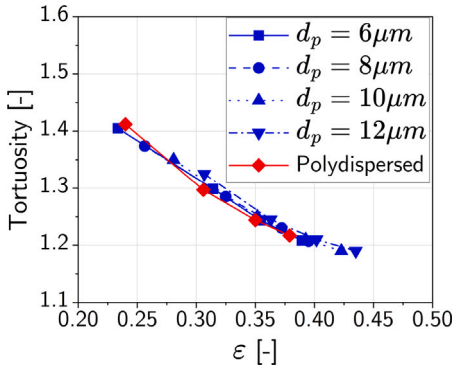

Fig. 13. Tortuosity as a function of the porosity for mono-disperse and polydisperse spherical particles.

for better LIB performance, it is best to keep the calendering degree around 20% with smaller particle sizes. For applications requiring high energy density, spherical particles might be considered despite their higher heat generation risks, provided thermal management is addressed. For high-power applications or scenarios with frequent fast charging, ellipsoidal particles may offer superior thermal stability due to better ion diffusion and heat dissipation characteristics. Optimal designs may involve blending both shapes to balance energy density and thermal performance effectively.

4. Concluding remarks

This study has investigated the effect of different calendering conditions on the behaviour of transport properties in porous LIB electrodes. Using the EEPA model and a bond model, the mechanical properties of electrode structures were conducted with DEM, and the behaviour of the electrolyte flow as a continuous phase was evaluated using pore-scale CFD simulations.

The electrode microstructures were built for different case studies, including mono-disperse and polydisperse spherical particles and mono-disperse ellipsoidal particles. In this study, the ellipsoidal particles were used as the oriented particles, to investigate the effect of anisotropy on the variation of tortuosity and permeability in different directions during calendering process. The multiple-sphere model, as a way to represent ellipsoidal particles in DEM, was employed. The following main conclusions can be drawn:

1. The porosity values for prolate particles used in this study were almost less than for spherical particles at each calendering degree. This behaviour can arise from the sphericity factor. It was also observed that the porosity reduction rate increases after 20% compression.
2. The mono-disperse and polydisperse spherical particles revealed isotropic behaviour in tortuosity and permeability for all calendaring degrees. The values of the tortuosity had approximately the same value at each porosity for all spherical morphologies. It was also observed that for all spherical morphologies, the values of the permeability had approximately the same value for the porosity values less than 0.35.
3. The results indicated that for the uncalendered structures, the diagonal components of tortuosity and permeability showed almost the same values for the all ellipsoidal particle sizes. The average inclination angle of ellipsoidal particles with respect to the horizontal plane, which is perpendicular to the applied force in the z direction decreased with increasing compression degree. This provides complicated path in the z direction, which resulted in more tortuosity and less permeability in the Z direction. The value of tortuosity in the z direction was about 5% more than the other directions. The value of permeability in the z direction was about 12% less. As the compression degree increased to 30%, the level of anisotropy was remarkably reduced.

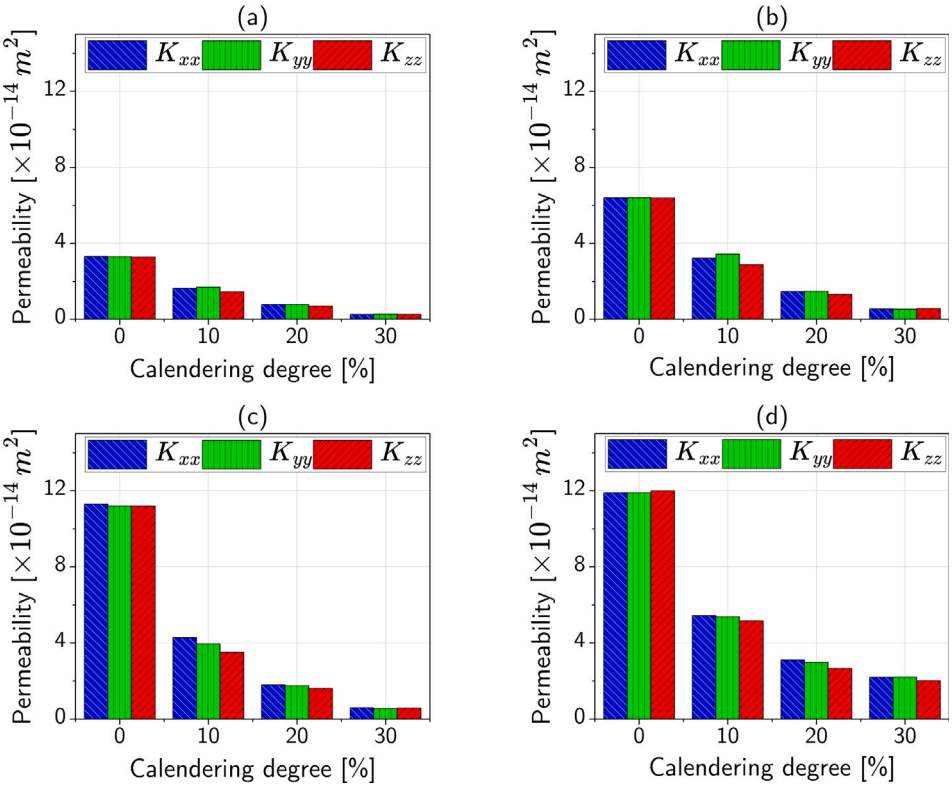

Fig. 14. Diagonal components of the permeability, K_{ii} under different calendering degrees. Short axis of ellipsoidal particles *a*: (a) 6 μm, (b) 8 μm, (c) 10 μm, and (d) 12 μm.

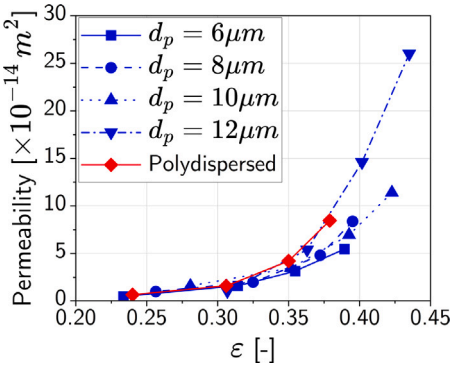

Fig. 15. Permeability as a function of the porosity for mono-disperse and polydisperse spherical particles.

4. The LIB electrochemical–thermal models show that it is best to keep the calendering rate around 20% with smaller particle sizes (for both spherical and ellipsoidal cases). Applying higher calendering degree can enhance the energy density of cells, however, it reduces the effective surface area and increases tortuosity, hindering Li-ion diffusion and negatively impacting power density. Moderate calendering may improve electrode wettability by rearranging particles and increasing divergence within pore networks. Conversely, excessive calendering decreases wettability due to reduced porosity and smaller average pore size. Therefore, the calendering process must be carefully optimised to produce electrodes with a balanced structure that ensures adequate electrical and ionic conductivities (and mechanical properties) ultimately enabling batteries with maximum volumetric energy density and extended cycle life.

CRediT authorship contribution statement

Siavash Sandooghdar: Writing – review & editing, Writing – original draft, Methodology, Data curation, Conceptualization. **Jiashen Chen:** Writing – review & editing, Software, Formal analysis. **Maryam Asachi:** Writing – review & editing, Supervision. **Ali Hassanpour:** Writing – review & editing, Supervision. **Elham Hosseinzadeh:** Formal analysis, Methodology, Software, Writing – review & editing. **Meisam Babaie:** Writing – review & editing, Supervision. **Masoud Jabbari:** Writing – review & editing, Supervision, Data curation, Conceptualization.

Declaration of competing interest

The authors declare that they have no known competing financial interests or personal relationships that could have appeared to influence the work reported in this paper.

Acknowledgements

For the purpose of open access, the author has applied a Creative Commons Attribution (CC BY) license to any Author Accepted Manuscript version arising from this submission.

Data availability

Data will be made available on request.

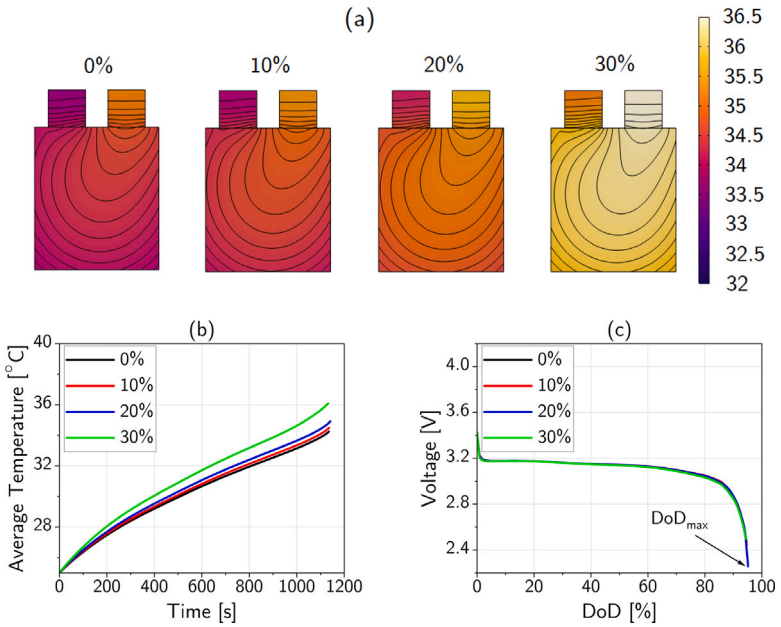

Fig. 16. The results of electrochemical-thermal model for the spherical particles of 6 μm and different calendering degrees showing (a) LIB surface temperatures, (b) LIB average cell temperature versus discharge time, and (c) the discharge curve showing voltage variation with respect to depth of discharge (DoD).

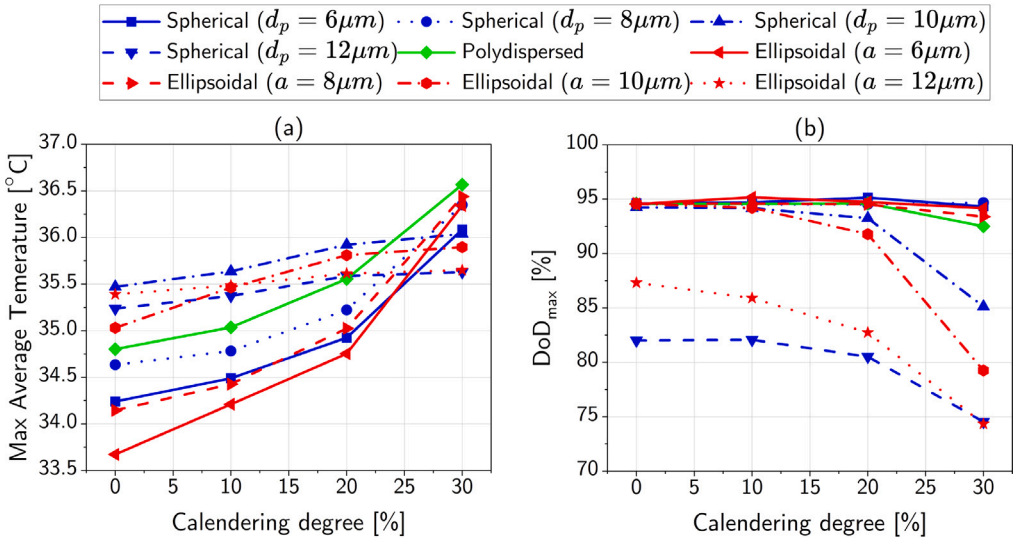

Fig. 17. Evolution of porosity under different calendering degrees.

References

[1] Y. Wang, B. Liu, Q. Li, S. Cartmell, S. Ferrara, Z.D. Deng, J. Xiao, Lithium and lithium ion batteries for applications in microelectronic devices: A review, J. Power Sources 286 (2015) 330–345.

[2] C. Meyer, H. Bockholt, W. Haselrieder, A. Kwade, Characterization of the calendering process for compaction of electrodes for lithium-ion batteries, J. Mater. Process. Technol. 249 (2017) 172–178.

[3] X. Lu, S.R. Daemi, A. Bertei, M.D. Kok, K.B. O'Regan, L. Rasha, J. Park, G. Hinds, E. Kendrick, D.J. Brett, et al., Microstructural evolution of battery electrodes during calendering, Joule 4 (12) (2020) 2746–2768.

[4] R. Ge, A.M. Boyce, Y. Sun, P.R. Shearing, P.S. Grant, D.J. Cumming, R.M. Smith, Numerical design of microporous carbon binder domains phase in composite cathodes for lithium-ion batteries, ACS Appl. Mater. Interfaces 15 (23) (2023) 27809–27820.

[5] M. Ademmer, B. Prifling, M. Weller, A. Hilger, M. Osenberg, I. Manke, V. Knoblauch, V. Schmidt, Investigating the influence of the calendering process on the 3D microstructure of single-layer and two-layer cathodes in lithium-ion batteries using synchrotron tomography, J. Power Sources 548 (2022) 231960.

[6] Y. Sheng, C.R. Fell, Y.K. Son, B.M. Metz, J. Jiang, B.C. Church, Effect of calendering on electrode wettability in lithium-ion batteries, Front. Energy Res. 2 (2014) 56.

[7] X. Lu, A. Bertei, D.P. Finegan, C. Tan, S.R. Daemi, J.S. Weaving, K.B. O'Regan, T.M. Heenan, G. Hinds, E. Kendrick, et al., 3D microstructure design of lithium-ion battery electrodes assisted by X-ray nano-computed tomography and modelling, Nature Commun. 11 (1) (2020) 2079.

[8] C.S. Giménez, B. Finke, C. Nowak, C. Schilde, A. Kwade, Structural and mechanical characterization of lithium-ion battery electrodes via DEM simulations, Adv. Powder Technol. 29 (10) (2018) 2312–2321.

[9] D. Zhang, W. Liu, C.-Y. Wu, Q. Cai, The development of a 3D pore-scale lattice Boltzmann model for 3D microstructure modeling and design of li-ion battery electrodes, Energy Technol. 10 (7) (2022) 2200080.

[10] J. Zhang, H. Huang, J. Sun, Investigation on mechanical and microstructural evolution of lithium-ion battery electrode during the calendering process, Powder Technol. 409 (2022) 117828.

[11] J. Zhang, J. Sun, H. Huang, Z. Yuan, Influence of calendering process on the structural mechanics and heat transfer characteristics of lithium-ion battery electrodes via DEM simulations, Particuology 85 (2024) 252–267.

[12] C.S. Giménez, B. Finke, C. Schilde, L. Froböse, A. Kwade, Numerical simulation of the behavior of lithium-ion battery electrodes during the calendaring process via the discrete element method, Powder Technol. 349 (2019) 1–11.
[13] A.C. Ngandjong, T. Lombardo, E.N. Primo, M. Chouchane, A. Shodiev, O. Arcelus, A.A. Franco, Investigating electrode calendering and its impact on electrochemical performance by means of a new discrete element method model: Towards a digital twin of Li-Ion battery manufacturing, J. Power Sources 485 (2021) 229320.
[14] R. Ge, D.J. Cumming, R.M. Smith, Discrete element method (DEM) analysis of lithium ion battery electrode structures from X-ray tomography-the effect of calendering conditions, Powder Technol. 403 (2022) 117366.
[15] S.J. Cooper, A. Bertei, P.R. Shearing, J. Kilner, N.P. Brandon, TauFactor: An open-source application for calculating tortuosity factors from tomographic data, SoftwareX 5 (2016) 203–210.
[16] T.-T. Nguyen, A. Demortière, B. Fleutot, B. Delobel, C. Delacourt, S.J. Cooper, The electrode tortuosity factor: why the conventional tortuosity factor is not well suited for quantifying transport in porous Li-ion battery electrodes and what to use instead, Npj Comput. Mater. 6 (1) (2020) 123.
[17] M. Ender, J. Joos, T. Carraro, E. Ivers-Tiffée, Quantitative characterization of LiFePO4 cathodes reconstructed by FIB/SEM tomography, J. Electrochem. Soc. 159 (7) (2012) A972.
[18] M. Safari, R. Gholami, M. Jami, M.A. Ananthan, A. Rahimi, W.S. Khur, Developing a porosity-permeability relationship for ellipsoidal grains: A correction shape factor for Kozeny-Carman's equation, J. Pet. Sci. Eng. 205 (2021) 108896.
[19] N. Conzelmann, M.N. Partl, F.J. Clemens, C. Müller, L.D. Poulikakos, Effect of artificial aggregate shapes on the porosity, tortuosity and permeability of their packings, Powder Technol. 397 (2022) 117019.
[20] V. Becker, O. Birkholz, Y. Gan, M. Kamlah, Modeling the influence of particle shape on mechanical compression and effective transport properties in granular lithium-ion battery electrodes, Energy Technol. 9 (6) (2021) 2000886.
[21] O. Birkholz, Y. Gan, M. Kamlah, Modeling the effective conductivity of the solid and the pore phase in granular materials using resistor networks, Powder Technol. 351 (2019) 54–65.
[22] P.A. Cundall, O.D. Strack, A discrete numerical model for granular assemblies, Geotechnique 29 (1) (1979) 47–65.
[23] Y. Gao, G. De Simone, M. Koorapaty, Calibration and verification of DEM parameters for the quantitative simulation of pharmaceutical powder compression process, Powder Technol. 378 (2021) 160–171.
[24] D. Yan, J. Yu, Y. Wang, L. Zhou, Y. Yu, A general modelling method for soybean seeds based on the discrete element method, Powder Technol. 372 (2020) 212–226.
[25] S.F. Sizkow, U. El Shamy, SPH-DEM simulations of saturated granular soils liquefaction incorporating particles of irregular shape, Comput. Geotech. 134 (2021) 104060.
[26] S.C. Thakur, H. Ahmadian, J. Sun, J.Y. Ooi, An experimental and numerical study of packing, compression, and caking behaviour of detergent powders, Particuology 12 (2014) 2–12.
[27] S.C. Thakur, J.P. Morrissey, J. Sun, J. Chen, J.Y. Ooi, Micromechanical analysis of cohesive granular materials using the discrete element method with an adhesive elasto-plastic contact model, Granul. Matter 16 (2014) 383–400.
[28] D. Schreiner, A. Klinger, G. Reinhart, Modeling of the calendering process for lithium-ion batteries with DEM simulation, Procedia CIRP 93 (2020) 149–155.
[29] D. Schreiner, J. Lindenblatt, R. Daub, G. Reinhart, Simulation of the calendering process of NMC-622 cathodes for lithium-ion batteries, Energy Technol. 11 (5) (2023) 2200442.
[30] T. Yano, S. Ohsaki, H. Nakamura, S. Watano, Compression properties of bimodal powders with different plasticities in the elastoplastic powder compression process: A numerical analysis, Adv. Powder Technol. 34 (12) (2023) 104245.
[31] A. Di Renzo, F.P. Di Maio, An improved integral non-linear model for the contact of particles in distinct element simulations, Chem. Eng. Sci. 60 (5) (2005) 1303–1312.
[32] O. Walton, Force models for particle-dynamics simulations of granular materials, Mob. Part. Syst. (1995) 367–380.
[33] M.J. Mohajeri, C. van Rhee, D.L. Schott, Replicating cohesive and stress-history-dependent behavior of bulk solids: Feasibility and definiteness in DEM calibration procedure, Adv. Powder Technol. 32 (5) (2021) 1532–1548.
[34] D.O. Potyondy, P.A. Cundall, A bonded-particle model for rock, Int. J. Rock Mech. Min. Sci. 41 (8) (2004) 1329–1364.
[35] F.L. Usseglio-Viretta, A. Colclasure, A.N. Mistry, K.P.Y. Claver, F. Pouraghajan, D.P. Finegan, T.M. Heenan, D. Abraham, P.P. Mukherjee, D. Wheeler, et al., Resolving the discrepancy in tortuosity factor estimation for Li-ion battery electrodes through micro-macro modeling and experiment, J. Electrochem. Soc. 165 (14) (2018) A3403–A3426.
[36] A. El Malki, M. Asch, O. Arcelus, A. Shodiev, J. Yu, A.A. Franco, Machine learning for optimal electrode wettability in lithium ion batteries, J. Power Sources Adv. 20 (2023) 100114.
[37] D. Schreiner, J. Lindenblatt, F.J. Günter, G. Reinhart, DEM simulations of the Calendering process: parameterization of the electrode material of Lithium-ion batteries, Procedia CIRP 104 (2021) 91–97.
[38] A. Khazeni, Z. Mansourpour, Influence of non-spherical shape approximation on DEM simulation accuracy by multi-sphere method, Powder Technol. 332 (2018) 265–278.
[39] D. Höhner, S. Wirtz, H. Kruggel-Emden, V. Scherer, Comparison of the multi-sphere and polyhedral approach to simulate non-spherical particles within the discrete element method: Influence on temporal force evolution for multiple contacts, Powder Technol. 208 (3) (2011) 643–656.
[40] S.-S. Lin, Y.-C. Chung, C.-K. Lin, Y.-C. Chen, DEM simulation and experimental validation for mechanical response of ellipsoidal particles under confined compression, Adv. Powder Technol. 29 (5) (2018) 1292–1305.
[41] A. Bejan, Convection Heat Transfer, John Wiley & Sons, 2013.
[42] A. Davoodabadi, J. Li, Y. Liang, D.L. Wood III, T.J. Singler, C. Jin, Analysis of electrolyte imbibition through lithium-ion battery electrodes, J. Power Sources 424 (2019) 193–203.
[43] M. Ebner, V. Wood, Tool for tortuosity estimation in lithium ion battery porous electrodes, J. Electrochem. Soc. 162 (2) (2014) A3064.
[44] B.L. Trembacki, A.N. Mistry, D.R. Noble, M.E. Ferraro, P.P. Mukherjee, S.A. Roberts, Mesoscale analysis of conductive binder domain morphology in lithium-ion battery electrodes, J. Electrochem. Soc. 165 (13) (2018) E725–E736.
[45] M.B. Clennell, Tortuosity: a guide through the maze, Geol. Soc. Spec. Publ. 122 (1) (1997) 299–344.
[46] E. Hosseinzadeh, J. Marco, P. Jennings, Electrochemical-thermal modelling and optimisation of lithium-ion battery design parameters using analysis of variance, Energies 10 (9) (2017) 1278.
[47] E. Hosseinzadeh, R. Genieser, D. Worwood, A. Barai, J. Marco, P. Jennings, A systematic approach for electrochemical-thermal modelling of a large format lithium-ion battery for electric vehicle application, J. Power Sources 382 (2018) 77–94.
[48] E. Hosseinzadeh, J. Marco, P. Jennings, The impact of multi-layered porosity distribution on the performance of a lithium ion battery, Appl. Math. Model. 61 (2018) 107–123.
[49] J. Li, Y. Cheng, L. Ai, M. Jia, S. Du, B. Yin, S. Woo, H. Zhang, 3D simulation on the internal distributed properties of lithium-ion battery with planar tabbed configuration, J. Power Sources 293 (2015) 993–1005.